DOI 10.24425/aee.2024.149926

Optimal control of maximum torque current ratio for synchronous reluctance motor based on virtual signal injection algorithm

JINGHUA CUI

The Department of Electrical Engineering, Hebei Chemical and Pharmaceutical College Shijiazhuang, 050026, China

e-mail: ✉ *cuijh2007@126.com*

(Received: 16.08.2024, revised: 18.04.2024)

Abstract: This study focuses on the maximum torque current ratio control of synchronous reluctance motors and proposes an optimized control method for the maximum torque current ratio of synchronous reluctance motors based on virtual signal injection. Firstly, the research on the maximum torque current ratio control of synchronous reluctance motors based on the virtual signal injection method is conducted, and the existing virtual unipolar square wave signal injection method is analyzed and studied. Secondly, a non-parametric maximum torque current ratio control strategy based on a synchronous reluctance motor combined with the virtual signal injection method is proposed. This strategy does not involve complex parameter calculations, and the control accuracy is not limited by the accuracy of the parameters in the model. The experimental results showed that under the control of virtual bipolar and unipolar square wave signal injection methods, the load torque was converted from 2 Nm to 6 Nm at $t = 2.5$ s, and there was a significant change in the current amplitude and waveform of the current vector. Under the control of the bipolar injection method, the current amplitude waveform of the motor was lower than that of the unipolar waveform, and the current was smaller. After the load suddenly changed, it could enter a stable state faster. After the load changed at $t = 2.5$ s, the phase angle of the current vector was quickly adjusted and stabilized under the control of the bipolar signal. The designed method has a good optimization effect compared to the traditional virtual signal injection method, and can achieve high-performance maximum torque current ratio optimization control on synchronous reluctance motors.

Key words: maximum torque current ratio control, parameter changes, synchronous reluctance motor, virtual signal injection method

1. Introduction

The synchronous reluctance motors (SynRMs) first emerged in the early 1920s as a type of motor that employs the salient polarity of the rotor to generate reluctance torque and drive rotation [1]. As the Industrial Revolution progressed, SynRM structures underwent constant optimization and improvement, and they have now found widespread usage and promotion in fields including fans and water pumps [2]. The SynRM has a simple structure, low cost, and is superior to switched reluctance motors in torque density, noise, vibration, efficiency, and other aspects [3]. The maximum torque per ampere (MTPA) control can effectively reduce motor losses and improve motor efficiency [4]. Inductance parameters are prominent in the MTPA control model and present nonlinear variations. As a result, achieving precise control of the MTPA in the SynRM becomes more challenging [5]. Therefore, this study proposes a SynRM-MTPA optimization control built on the virtual signal injection method (VSIM) to address the significant non-linear changes in SynRM parameters caused by factors such as inductance saturation and temperature. The objective is to improve the operational efficiency of the motor by increasing power density. The content is mainly divided into five parts. The first part is the introduction, which elaborates on the current research status of the SynRM and MTPA control, and provides an overview of the organizational structure of this paper. The second part is a literature review on the application of SynRM and VSIM algorithms in various fields, as well as the research results of many scholars in this field. The third part analyzes the nonlinear characteristics of inductance parameters in the SynRM, proposes and studies the optimization control of the SynRM-MTPA based on the VSIM algorithm. The first section is about studying the control of the SynRM-MTPA by combining the VSIM. The second section describes the MTPA strategy in accordance with SynRM-VSIM parameters. The fourth part demonstrates the accuracy of SynRM-MTPA optimization control under the VSIM algorithm through comparative experimental analysis, and evaluates its effectiveness. The fifth part is a summary and outlook on the research methods and results of this study.

2. Related work

The VSIM uses mathematical models as the core to calculate the torque value of high-frequency signal injection, and its calculation method is simple. Therefore, many scholars have conducted extensive research on it. Antonietti *et al*. designed a coordinated virtual element method for numerical approximation of two-dimensional elastodynamic problems, and derived the optimal error estimate under the energy and L2 norm. The method was assessed on various computational grids, featuring non-convex elements of up to the fourth order in h-refinement settings. Both semi-discrete and fully-discrete schemes were subjected to dispersion and dissipation analyses. Polygonal grids exhibited classic single quadrilateral grids in terms of dispersion and dissipation characteristics [6]. Zhang *et al*. proposed a cross domain virtual network embedding (VNE) algorithm for the space-air-ground integrated network (SAGIN), which models distinctive net-pieces of the SAGIN and sets net-attributes based on the realistic situation and user needs of the SAGIN. They constructed a feature matrix from the extracted network attributes and used it as a training environment. This algorithm had effectiveness. The SAGIN was more flexible with a wider coverage range and higher seamless connection quality [7].

The SynRM does not have the same magnet as traditional machines and is not subject to fluctuations in rare earth material prices. Additionally, there is no risk of demagnetization, which has prompted numerous scholars to investigate and produce many experimental results. Naseer *et al*. proposed an analytical modeling technique based on modified winding functions and common energy analysis to describe the characteristics of the SynRM. This model successfully provided the average torque and torque distribution of the SynRM under magnetic linear and nonlinear conditions, as a function of input current and load angle. This modeling technique only required a small portion of the simulation run time and accurately calculated the minimum requirements for resources and simulation time [8]. Qu *et al*. proposed an improved 2V-MPTC, which establishes torque and flux deadbeat control and optimizes the duty cycle to calculate the reference voltage vector. Compared with previous methods, this algorithm had better computational efficiency and could significantly reduce torque ripple [9]. Pasqualotto and Zigliotto proposed a huge sized training dataset produced by combining a tuned motion model with some data augmentation techniques. It is a convolutional neural network (CNN) that underwent training using a secure and cost-effective simulation dataset. Moreover, it underwent a thorough testing phase, wherein it was evaluated on both healthy and defective permanent magnet synchronous motors (PMSMs). The universality of the dataset also paved the way for detecting other faults and applying it to various motors [10]. Yao *et al*. studied the selection criteria for design tolerances for laser cutting machines and selected an appropriate tolerance range to meet thrust performance and low manufacturing costs. Firstly, they analyzed and determined the relationship between air gap geometric tolerances and thrust performance, and then introduced extreme learning machines into high-precision and high-efficiency thrust modeling. This method optimized the effectiveness of tolerance selection [11]. Liu *et al*. proposed a hybrid material with a permanent magnet synchronous linear motor (PMSLM) structure, which was optimized and designed using ferrite at the edges. It utilized the simulation results of air gap magnetic flux density distribution, back electromotive force, and cogging force to compare their configurations and their relative advantages and disadvantages. The hybrid magnet structure PMSLM had better magnetic properties, and compared to traditional machine structures, the cost of magnet materials had been reduced by nearly 25% [12].

In summary, the VSIM mainly uses mathematical models to calculate the torque value after high-frequency signal injection, and automatically introduces harmonics during the control process, which has good control effects. However, this method has difficulties in controlling nonlinear changes in motor parameters and relies to some extent on the estimated values of errors. Therefore, this study proposes SynRM-MTPA optimization control based on the VSIM algorithm to address the nonlinear characteristics of parameters that the traditional VSIM cannot consider. This optimization is carried out through error quantification analysis, thereby improving the efficiency of the motor.

3. Optimization control of SynRM based on VISM algorithm

In the early development of the SynRM, the reluctance torque that causes the motor to rotate was generated by utilizing the salient polarity of the rotor. After long-term improvement, it is extensively utilized in water pumps and fans [13]. The parameters of the SynRM exhibit significant

nonlinear changes under factors such as magnetic saturation and temperature, and the VSIM can effectively control this change [14]. To improve the operational efficiency of the motor, this study focuses on MTPA control.

3.1. SynRM-MTPA control based on VSIM

The SynRM does not have permanent magnets inside its rotor, which is different from the PMSM. Its rotor structure mostly adopts a multi-layer magnetic barrier shape. In the SynRM rotor structure, there are two symmetrical axes corresponding to the direction of low magnetic resistance and the direction of high magnetic resistance [15]. Most of the current AC motor MTPA control methods are primarily grounded on PMSM research. Therefore, to make a difference, this study sets the direction of the larger magnetic resistance as the d axis and the smaller direction as the q-axis. Figure 1 shows the rotor structure of the SynRM.

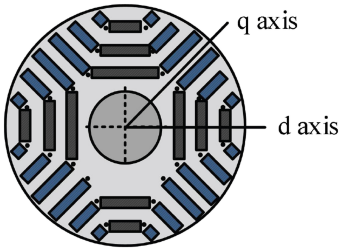

Fig. 1. The rotor structure of SynRM

The three-phase AC sine wave current is applied to the stator side of the three-phase SynRM, generating a circular rotating magnetic field inside the motor. Due to the absence of permanent magnets in the SynRM, the magnitude of the torque generated is positively correlated with the distinction in inductance between the d and q axes, so it is recognized as reluctance torque [16]. The expression for the three-phase stator (3PS) reluctance of the SynRM in a stationary three-phase coordinate system (S3P-CS) is shown in Eq. (1).

$$\begin{bmatrix} \psi_a \\ \psi_b \\ \psi_c \end{bmatrix} = \begin{bmatrix} L_a & M_{ab} & M_{ac} \\ M_{ba} & L_b & M_{bc} \\ M_{ca} & M_{cb} & L_c \end{bmatrix} \begin{bmatrix} i_a \\ i_b \\ i_c \end{bmatrix}. \tag{1}$$

In Eq. (1), L_a, L_b, and L_c are the self inductance of 3PS windings. M_{ab}, M_{ac}, M_{ba}, M_{bc}, M_{ca}, and M_{cb} are the mutual inductance between 3PS windings. In the actual operation of the motor, due to the influence of manufacturing error, material non-uniformity, magnetic saturation phenomenon and other factors, the inductance conductance will change with the rotor angle to a certain extent. At high currents or frequencies, magnetic saturation and skin effects can cause a significant change in inductance. Therefore, it is necessary to analyze the design and working state of the motor. Under the S3P-CS, the stator voltage equation of synchronous reluctance is Eq. (2).

$$\begin{bmatrix} u_a \\ u_b \\ u_c \end{bmatrix} = \begin{bmatrix} R & 0 & 0 \\ 0 & R & 0 \\ 0 & 0 & R \end{bmatrix} \begin{bmatrix} i_a \\ i_b \\ i_c \end{bmatrix} + p \begin{bmatrix} \psi_a \\ \psi_b \\ \psi_c \end{bmatrix}. \tag{2}$$

In Eq. (2), u_a, u_b, and u_c are the 3PS winding phase voltages of the SynRM, respectively. i_a, i_b and i_c represent the 3PS winding phase currents. ψ_a, ψ_b and ψ_c are three-phase magnetic links. R is the stator winding resistance. p is a differential operator. According to the principle of electromechanical energy conversion, the expression of electromagnetic torque and magnetic co-energy of the motor is shown in Eq. (3).

$$\begin{cases} T_e = \dfrac{\partial W_m}{\partial \theta_m} = P\dfrac{\partial W_m}{\partial \theta} = \dfrac{P}{2}[I]^T \dfrac{\partial [I]}{\partial \theta}[I] \\ W_m = \dfrac{1}{2} \times \dfrac{B_n}{2} \times V_n \end{cases}. \tag{3}$$

In Eq. (3), W_m represents the total magnetic energy of the entire motor. θ_m means the mechanical angular displacement of the rotor. θ is the corresponding electrical angle. P is the quantity of motor poles. B_n is the strength of the magnetic field, and V_n is the volume of the object. The expression of the motor motion is Eq. (4).

$$T_e = J\frac{\mathrm{d}\omega_m}{\mathrm{d}t} + B_m\omega_m + T_L. \tag{4}$$

In Eq. (4), T_L is the load torque, ω_m represents the mechanical angular velocity of the rotor, J represents the rotational inertia, and B_m represents the friction coefficient. However, in practical situations, the inductance parameters are easily affected by factors such as saturation effects in the motor's magnetic circuit and changes in temperature, resulting in non-linear changes [17]. This study uses torque model reconstruction and numerical calculation to extract the MTPA criterion. In addition, a virtual unipolar square wave signal (VUSWS) with a duty cycle of 50% is used as the injection signal, as shown in Eq. (5).

$$\Delta\beta = \begin{cases} 0, & kT_s \le t < (k+0.5)T_s \\ \delta, & (k+0.5)T_s \le t < (k+1)T_s \end{cases}. \tag{5}$$

In Eq. (5), δ and T_s respectively, represent the amplitude and period of the square wave signal during the k-th virtual signal injection, $k = 1, 2, 3, \ldots$, δ represents a small positive polarity constant. As a constant, the value of T_s is much smaller than the period of the three-phase sinusoidal alternating current of the motor. The electromagnetic torque T_e^h injected with a VUSWS is Taylor expanded at β, but due to the small value of δ, derivative terms above the second order can be ignored. Therefore, the expression of the electromagnetic torque after injecting the VUSWS is shown in Eq. (6).

$$T_e^h = T_e(\beta+\delta) = T_e(\beta) + \frac{\partial T_e}{\partial \beta}\delta. \tag{6}$$

$\partial T_e/\partial\beta$ in Eq. (6) is obtained through Eq. (7).

$$\frac{\partial T_e}{\partial \beta} = \frac{T_e^h - T_e}{\delta}. \tag{7}$$

In Eq. (7), T_c represents the Dai Nianzi torque before injecting the phase angle offset signal. Thus, in VUSWS injection, the criterion $\partial T_e/\partial\beta$ for controlling the motor to operate at the MTPA point can be obtained only by knowing the electromagnetic torques T_e^h and T_e before and after the injection signal. Figure 2 shows the working process of the MTPA on the basis of the VUSWS method.

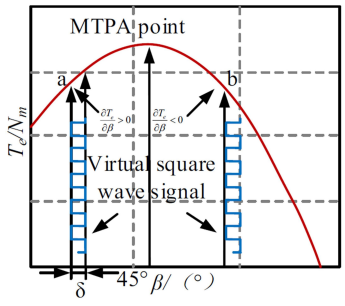

Fig. 2. Working principle of virtual unipolarity injection method

The virtual square wave signal injection method obtains T_e^h through torque model reconstruction and numerical calculation, and follows the data of inductance L_d and L_q on the d and q axes, as well as obtaining i_d^h and i_q^h through calculation. In addition, the stator currents (SCs) i_d^h and i_q^h of d and q based on the characteristics of the square wave signal is linearized. In the process of signal injection and electromagnetic torque model reconstruction, the dynamic characteristics of L_{dd}, L_{qq} and L_{dq} also need to be accurately grasped. The injected virtual signal will produce additional dynamic magnetic field effects in the motor, which may cause these inductance parameters to change with the rotor position. In addition, the inductance parameters L_{dd}, L_{qq}, L_{dq} in synchronous reluctance motors will also change significantly due to the non-linearity of the motor magnetic circuit, temperature fluctuations, and magnetic saturation effects. Therefore, the identification and quantification of inductance parameters L_{dd}, L_{qq} and L_{dq} is the key to ensure accurate control when the MTPA operation point is calculated by the signal injection method. By considering these dynamic characteristics comprehensively in the design of the motor control algorithm, the corresponding compensation mechanism is introduced to adapt to the change of inductance parameters, so as to ensure that the motor can operate efficiently according to the principle of the MTPA under various operating conditions. In the model, the d and q inductance parameters L_d and L_q of the motor are constant. The calculation formulas for the inductance L_d and L_q of d and q are in Eq. (8).

$$\begin{cases} L_d = \dfrac{u_{q\text{ref}} - Ri_q}{P\omega_m i_d} \\ L_q = -\dfrac{u_{d\text{ref}} - Ri_d}{P\omega_m i_q} \end{cases}. \tag{8}$$

In Eq. (8), in the vector control system, the d-axis and q-axis voltages u_d and u_q represent the given voltages $u_{d\text{ref}}$ and $u_{q\text{ref}}$. ω_m represents the motor speed. i_d and i_q represent the SC of d and q. The expressions for the SCs i_d^h and i_q^h of d and q after linearization based on the characteristics of the square wave signal are shown in Eq. (9).

$$\begin{cases} i_d^h = -I_m \sin(\beta + \delta) \approx i_d - i_q\delta \\ i_q^h = I_m \cos(\beta + \delta) \approx i_q + i_d\delta \end{cases}. \tag{9}$$

In Eq. (9), $\partial T_e/\partial\beta > 0$ can be extracted, if the phase angle of the motor current vector is less than the MTPA point, the calculated torque T_e^h is greater than the previous torque T_e after the phase angle is shifted forward. Therefore, it is necessary to control the increase in the current

phase angle and vice versa. The overall framework of the VUSWS injection method motor system is obtained by adjusting the control logic of the current phase angle according to the $\partial T_e/\partial\beta$ criterion above, as shown in Fig. 3.

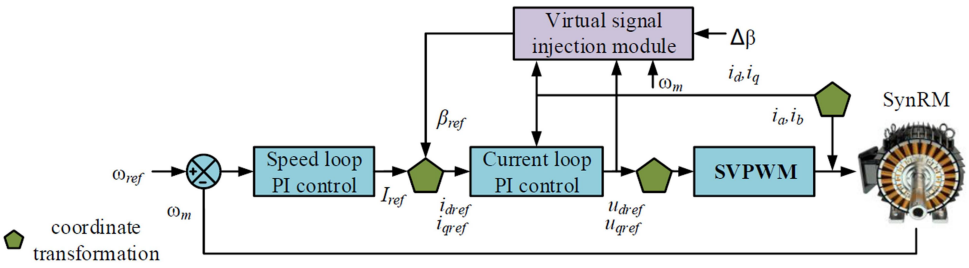

Fig. 3. Framework diagram of virtual square wave signal injection method system

The system adopts speed current dual closed-loop control, and the first step is to calculate the difference between the given speed and the actual motor speed; the second step is to use the speed loop PI to control the given current vector amplitude I_{ref}; the third step is to use the VSIM to determine the given current vector phase angle B_{ref}, and finally, to achieve SVPWM control of the SynRM. The VUSWS method is used to construct the overall framework of electromagnetic torque after injecting phase angle offset signals, without the need to truly introduce cheap phase angle signals into the system, which compensates for the inherent shortcomings of the real signal injection method [18, 19].

3.2. SynRM-MTPA control strategy based on VSIM parameters

When modeling a SynRM, the magnetic saturation of the motor is an important consideration [20, 21]. Due to magnetic saturation, the motor's parameters will undergo non-linear changes before and after virtual signal injection, leading to reduced model accuracy and adversely affecting the control algorithm's accuracy [22]. Additionally, the correlation between inductance and flux must account for current dependence since inductance typically changes with current changes [23]. To solve this problem, the VUSWS injection method is optimized to obtain the virtual bipolar square wave signal injection method. This optimization process can dynamically quantify the inductance parameter variables, so as to realize the precise control of the MTPA of the SynRM. In this way, the accuracy of inductance parameters in the model can be improved, and the control effect of the algorithm can be enhanced. Among them, the overall framework of virtual bipolar square wave signal injection (VBSWSI) is roughly the same as that of the VUSWS injection method, and Fig. 4 shows the Current Vector Phase Angle Control Module (CVPACM) under this method.

By integrating the bipolar characteristics of sine wave signals and the advantages of square wave signals, this control module offers faster dynamic response speed and higher steady-state accuracy. The definition of the VBSWS is Eq. (10).

$$\Delta\beta = \begin{cases} -\delta, & kT_s \le t < (k+0.5)\,T_s \\ \delta, & (k+0.5)T_s \le t < (k+1)T_s \end{cases}. \tag{10}$$

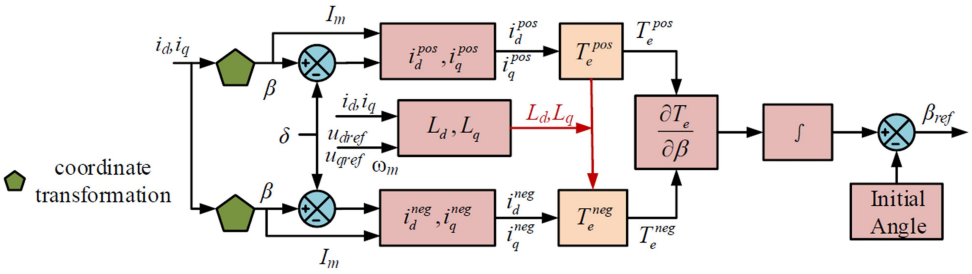

Fig. 4. VBSWSI method's CVPACM

In Eq. (10), $k = 1, 2, 3, \ldots$ δ and T_s represent the amplitude and period of the bipolar square wave signal at the k-th VSIM. The extraction formula of $\partial T_e/\partial\beta$ in VBSWSI is Eq. (11).

$$\frac{\partial T_e}{\partial \beta} = \frac{T_e^{\text{pos}} - T_e^{\text{neg}}}{2\delta}. \tag{11}$$

In Eq. (11), T_e^{pos} represents the electromagnetic torque of the virtual positive square wave signal, and T_e^{neg} represents the electromagnetic torque of the virtual negative square wave signal. The electromagnetic torques T_e^{pos} and T_e^{neg} are expanded by Taylor expansion at β, respectively. Due to the small size of δ, derivative terms above the second order are ignored, and their expressions are obtained as Eq. (12).

$$\begin{cases} T_e^{\text{pos}} = T_e + \dfrac{\partial T_e}{\partial \beta}\delta \\ T_e^{\text{neg}} = T_e - \dfrac{\partial T_e}{\partial \beta}\delta \end{cases}. \tag{12}$$

By adjusting the control logic of the current phase angle based on the criterion $\partial T_e/\partial\beta$ above, the extracted MTPA criterion $\partial T_e/\partial\beta$ is integrated to optimize the current vector phase angle. When calculating $\partial T_e/\partial\beta = 0$ again, the motor stabilizes at the MTPA point. Figure 5 shows the working principle of the VBSWS.

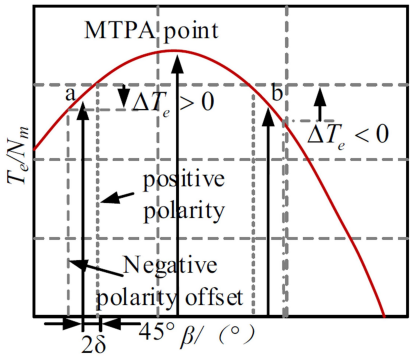

Fig. 5. Working principle of VBSWS method

In Fig. 5, at point a, when the motor current phase angle is less than the MTPA, if the torque value calculated after the positive polarity offset of the phase angle is greater than the negative polarity offset, then $\partial T_e/\partial\beta > 0$. Similarly, at point b, if the calculated value is small, then the phase angle of $\partial T_e/\partial\beta < 0$ and the current vector decreases. Therefore, the VBSWS method can stabilize the motor at the MTPA point. However, in the algorithm, it is also necessary to consider the nonlinear variation of SynRM inductance parameters, and the expression of the electromagnetic torque T_e^{pos} of its virtual positive polarity square wave signal is Eq. (13).

$$T_e^{\text{pos}} = \frac{3}{2}P\left[(L_d^{\text{pos}} - L_q^{\text{pos}})i_d^{\text{pos}} i_q^{\text{pos}}\right]. \tag{13}$$

In Eq. (13), i_d^{pos} represents the SC of the d-axis in the virtual positive electrode, and i_q^{pos} represents the SC of the q-axis in the virtual positive electrode. Due to the vector control adopted by VBSWSI, the torque calculation formula for the corrected injected virtual positive polarity square wave signal is Eq. (14).

$$T_e^{\text{pos}} = \frac{3}{2\omega_m}P\left[\frac{u_{d\text{ref}} - Ri_d}{i_q} i_d^{\text{pos}} i_q^{\text{pos}} + (u_{q\text{ref}} - Ri_q - P\omega_m L_d i_q \delta) i_q^{\text{pos}}\right]. \tag{14}$$

In Eq. (14), $u_{d\text{ref}}$ and $u_{q\text{ref}}$ represent the voltage of the given d and q axes, respectively. ω_m represents the motor speed. i_d and i_q are the SCs of the d and q axes, respectively, which can be obtained through measurement. Similarly, the torque calculation formula for the modified injection method virtual negative polarity square wave signal is Eq. (15).

$$T_e^{\text{neg}} = \frac{3}{2\omega_m}P\left[\frac{u_{d\text{ref}} - Ri_d}{i_q} i_d^{\text{neg}} i_q^{\text{neg}} + (u_{q\text{ref}} - Ri_q + P\omega_m L_d i_q \delta) i_q^{\text{neg}}\right]. \tag{15}$$

In different application scenarios of motors and working conditions, the steady-state control accuracy and the discrimination of working condition changes depend on the threshold [24, 25]. Therefore, this study designed a bidirectional incremental inductance detection mechanism (BIIDM) to adaptively adjust the direction and step size of inductance parameters for application scenarios. Therefore, based on the design of VBSWSI, the working principle of the BIIDM is Fig. 6.

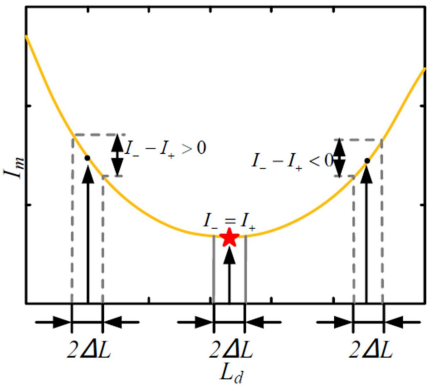

Fig. 6. Principle of BIIDM

The red star shaped icon in Fig. 6 shows the MTPA operating point of the motor. When L_d in the current torque model is less than the optimal inductance parameter, i.e. $I_- - I_+ > 0$, L_d increases and moves towards the MTPA point direction. On the contrary, when L_d of the current torque model is greater than the optimal inductance parameter, i.e. $I_- - I_+ < 0$, L_d decreases and moves towards the MTPA point. When the motor runs to the MTPA point, the current amplitudes on both sides of the working point remain basically the same, that is, when $I_- = I_+$ is reached, L_d is no longer updated, and the optimization of the optimal inductance parameters is completed [26]. The BIIDM is adjusted based on the difference in current amplitude on both sides of the working point. Therefore, this control strategy is capable of making adaptive adjustments in response to changes in working conditions, enabling easy transportability across different motors, and hence exhibits high flexibility [27, 28].

4. Optimal control simulation of maximum torque current ratio of SynRM based on VSIM algorithm

To validate the traditional VUSWS injection method, simulation experiments were conducted with improved VBSWSI and inductance parameter scanning. In the experiment, the parameters of the controlled motor and the experimental motor remain consistent. Furthermore, setting the inductance parameters of the motor model as constants is the only viable option. The corresponding parameters for the d and q inductance parameter data in the model can be searched for and output to achieve a complete simulation of the nonlinear variation characteristics of SynRM inductance parameters. The information for the d-axis and q-axis parameters is obtained from Table 1 through finite element simulation of the experimental motor.

Table 1. Synchronous reluctance motor parameters

Symbol	Parameter	Numerical value
I_m	Rated current (effective value) (A)	18.6
T_n	Rated torque (Nm)	12
n_n	Rated speed (r/min)	2 200
P	Number of motor poles	5
R_s	Stator phase resistance (Ω)	0.5
L_d	d-axis inductance (H)	0.00467–0.01076
L_q	q-axis inductance (H)	0.01118–0.02274
Other	Winding connection method	Star join

Combining the parameters in Table 1 with the theory of the SynRM model, VBSWSI produces a given vector phase angle value. Due to the fact that the VSIM does not truly cause current vector phase angle drift, the MTPA control criterion $\partial T_e / \partial \beta$ can be obtained through numerical calculation. After further calculation, the given value of the current vector phase angle can be

obtained. When the system is stable, the phase angle of the output current vector remains stable, meeting $\partial T_e/\partial\beta = 0$, and the motor is also operating at the MTPA operating point. Since the VSIM does not actually inject phase angle offset signals into the system, it will not cause any extra losses or noise. Therefore, at a speed of 600 r/min, the steady-state sinusoidal three-phase current results of the motor under strategic control under 2 Nm light load and 8 Nm heavy load conditions are shown in Fig. 7.

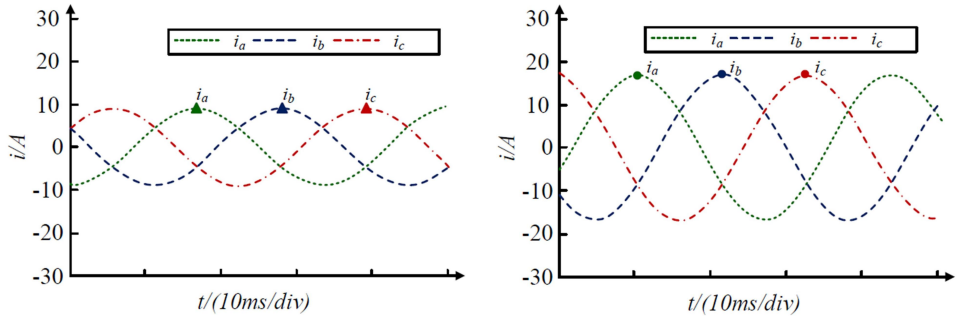

Fig. 7. Simulation waveform of three-phase current with age controlled by VBSWSI method for (a) 2 Nm and (b) 8 Nm

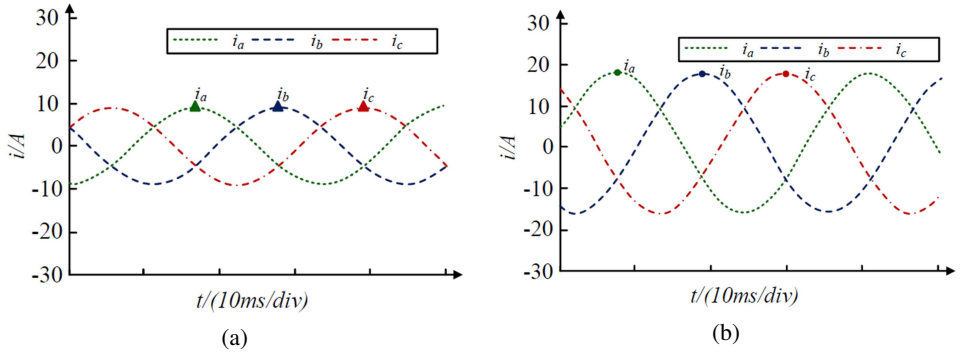

Fig. 8. Three phase current simulation waveform of motor controlled by inductance parameter scanning method for (a) 2 Nm and (b) 8 Nm

In Fig. 8, there is a small difference between the steady-state current fluctuation amplitude of the motor under the control of this method and the control effect of VBSWSI. From Fig. 8(a), under a light load condition of 2 Nm, the relationship curve between the A-MCV and the PA-CV is in a flat state, and the effect of observing current changes is not significant, with slightly lower accuracy. According to Fig. 8(b), under the heavy load condition of 8 Nm, the curve is steep, and its control accuracy judgment speed is faster than VBSWSI. In the steady-state performance simulation experiment, the motor is set to a given speed of 600 r/min, while the load torque is set to 2 Nm, 4 Nm, 6 Nm, and 8 Nm. To observe its performance more intuitively, the simulation results of the motor under the control strategy were compared, and Table 2 shows the results.

Table 2. Simulation results of SynRM steady-state current value at a speed of 600 r/min

Load torque/Nm	**VUSWSI method/A**	**VBSWSI method/A**	**Inductance parameter scanning method/A**	**VSIM/A based on isomorphic inductance torque model**
2.0	9.24	9.18	9.15	9.15
4.0	13.03	12.01	11.94	11.94
6.0	14.69	14.52	14.29	14.32
8.0	17.58	17.09	16.49	16.51

From Table 2, under the same load torque, the steady-state current of the motor under VBSWSI control is smaller than that under traditional VUSWSI control. As the load increases, the difference in the steady-state operating current of the motor under the control of the two methods also increases. From this, the VBSWS can optimize traditional VUSWSI to eliminate the inherent steady-state errors of traditional methods and improve the steady-state accuracy of MTPA control. To verify the transient performance of the proposed algorithm, the motor operates at a given speed of 600 r/min and the load torque is converted from 2 Nm to 6 Nm. The waveform changes of the motor's current amplitude and current vector phase angle are observed. Figure 9 shows the comparison results with VUSWSI.

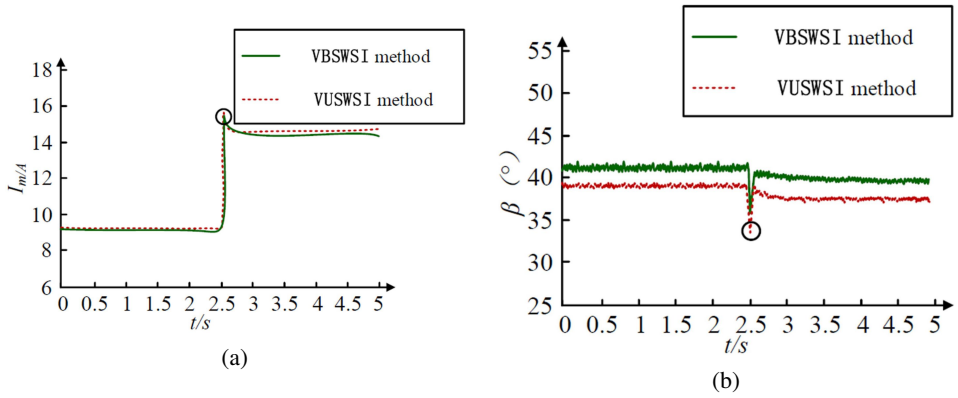

Fig. 9. Simulation results of VBSWSI method under 600 r/min variable load: (a) current amplitude I_m waveform, (b) current vector phase angle β waveform

From Fig. 9, under the control of VBSWSI and VUSWSI, the load torque is converted from 2 Nm to 6 Nm at $t = 2.5$ s, and there is a significant change in the current amplitude and waveform of the current vector. From Fig. 9(a), the current amplitude waveform of the motor under VBSWSI control is lower than that of the unipolar square wave injection method, and the current is smaller. After a sudden load change, it can enter a stable state faster. From Fig. 9(b), after the load changes

at t = 2.5 s, the current vector phase angle is quickly adjusted and stabilized under VBSWSI control, verifying the good dynamic response performance of the algorithm. At the same given speed, the load torque is converted from 2 Nm to 6 Nm at t = 2.5 s. The waveform changes of the current amplitude and current vector under the scanning method of motor inductance parameters and VUSWSI control were observed. The results are shown in Fig. 10.

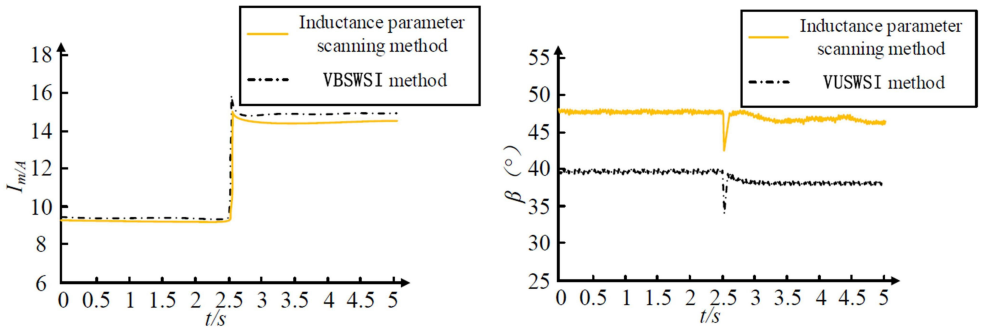

(a) (b)

Fig. 10. Simulation results of inductance parameter scanning method under 600 r/min variable load: (a) current amplitude I_m waveform, (b) current vector phase angle β waveform

From Fig. 10, under the inductance parameter scanning method and VUSWSI control, the load torque is converted from 2 Nm to 6 Nm at t = 2.5 s, and there is a significant change in the current amplitude and waveform of the current vector. From Fig. 10(a), compared to VUSWSI, the current amplitude is smaller under the control of the inductance parameter scanning method. As the load transitions, the optimization effect of the algorithm becomes more apparent as the inductance scanning method optimizes the inductance parameters of the torque model for the optimal inductance value. Based on Fig. 10(b), the PA-CV under control of the inductance parameter scanning method requires an adjustment period following sudden load changes in order to achieve stability, accompanied by minor oscillation amplitude. This is because the BIIDM causes a relatively small oscillation of the phase angle near the MTPA point. So, the inductance parameter scanning method has good dynamic response performance.

5. Conclusion

In recent years, the VSIM has become one of the focuses of attention in implementing MTPA control, but due to the algorithm treating motor parameters as constants, the nonlinear changes in motor parameters are very significant. Therefore, precise MTPA control cannot be achieved on the SynRM. This study aimed to address this issue by optimizing the traditional VSIM algorithm and implementing MTPA strategy control based on non-parametric dependencies. The results indicated that when the system was stable, the phase angle of the output current vector remained stable, and $\partial T_e/\partial\beta = 0$ was met, and the motor operated at the MTPA operating point. Due to the fact that the VSIM did not truly inject phase angle offset signals into the system, it would not generate

additional losses and noise. Under the control of this method, the steady-state current of the motor was almost stable. Under a light load condition of 2 Nm, the relationship curve between the A-MCV and the PA-CV was flat. Therefore, the effect of using scanning method to observe current changes nearby was not significant, and the accuracy was slightly lower. Under 8 Nm heavy-duty working conditions, the relationship curve between the A-MCV and the PA-CV was relatively steep. Therefore, the scanning method could fully utilize its advantages and improve its control accuracy. Under the same load torque, the steady-state current of the motor under VBSWSI control was smaller than that under traditional VUSWSI control. As the load increased, the difference in steady-state operating current of the motor under the control of the two methods also increased. Thus, the VBSWS can optimize traditional VUSWSI to eliminate inherent steady-state errors in traditional methods and improve the steady-state accuracy of MTPA control. However, the MTPA control strategy that is independent of parameters belongs to a search method category. Nonetheless, it still necessitates a considerable time frame to enhance the amplitude of the square wave signal as well as the intermediate variables upon encountering sudden variations in the operating conditions. Hence, additional research and exploration of dynamic optimization speed are necessary in the future.

References

[1] Danjuma M.U., Yusuf B., Yusuf I., *Reliability, availability, maintainability, and dependability analysis of cold standby series-parallel system*, Journal of Computational and Cognitive Engineering, vol. 1, no. 4, pp. 193–200 (2022), DOI: 10.47852/bonviewJCCE2202144.

[2] Park J.S., Kim J.M., Barlat F., Lim J.H., Pierron F., Kim J.H., *Characterization of dynamic hardening behavior at intermediate strain rates using the virtual fields method*, Mechanics of Materials, vol. 162, no. 4, 104101 (2021), DOI: 10.1016/j.mechmat.2021.104101.

[3] Liu Y., Shu S., Wei H.Y., Yang Y., *A virtual element method for the steady-state Poisson-Nernst-Planck equations on polygonal meshes*, Computers and Mathematics with Applications, vol. 102, no. 15, pp. 95–112 (2021). DOI: j.camwa.2021.10.002.

[4] Wu C.L., Zhang L.L., Song G., Yin H.M., *Inclusion-based boundary element method for virtual experiments of particulate composites containing arbitrarily shaped inhomogeneities*, Engineering Analysis with Boundary Elements, vol. 135, no. 1226, pp. 93–114 (2022), DOI: 10.1016/j.enganabound.2021.10.024.

[5] Wu C.L., Yin H.M., *The inclusion-based boundary element method (iBEM) for virtual experiments of elastic composites*, Engineering Analysis with Boundary Elements, vol. 124, no. 1226, pp. 245–258 (2021), DOI: 10.1016/j.enganabound.2020.12.020.

[6] Antonietti P.F., Manzini G., Mazzieri I., Mourad H.M., Verani M., *The arbitrary-order virtual element method for linear elastodynamics models: convergence, stability and dispersion-dissipation analysis*, International Journal for Numerical Methods in Engineering, vol. 122, no. 4, pp. 934–971 (2021), DOI: 10.1002/nme.6569.

[7] Zhang P.Y., Wang C., Kumar N., Liu L., *Space-air-ground integrated multi-domain network resource orchestration based on virtual network architecture: a DRL method*, IEEE Transactions on Intelligent Transportation Systems, vol. 23, no. 3, pp. 2798–2808 (2022), DOI: 10.1109/TITS.2021.3099477.

[8] Naseer M.U., Kallaste A., Asad B., Vainmann T., Rassolkin A., *Analytical modelling of synchronous reluctance motor including non-linear magnetic condition*, IET Electric Power Applications, vol. 16, no. 4, pp. 511–524 (2022), DOI: 10.1049/elp2.12172.

[9] Qu J.Z., Jatskevich J., Zhang C.N., Zhang S., *Improved multiple vector model predictive torque control of permanent magnet synchronous motor for reducing torque ripple*, IET Electric Power Applications, vol. 15, no. 5, pp. 681–695 (2021), DOI: 10.1049/elp2.12050.

[10] Pasqualotto D., Zigliotto M., *A comprehensive approach to convolutional neural networks-based condition monitoring of permanent magnet synchronous motor drives*, IET Electric Power Applications, vol. 15, no. 7, pp. 947–962 (2021), DOI: 10.1049/elp2.12059.

[11] Yao Z., Zhao J., Song J., Dong P., He Z.Y., Zong K.F., *Research on selection criterion of design tolerance for air-core permanent magnet synchronous linear motor*, Transactions on Industrial Electronics, vol. 68, no. 4, pp. 3336–3347 (2021), DOI: 10.1109/TIE.2020.2979574.

[12] Liu X.M., Yu H.T., Gerada D., Xu Z.Y., Qiu H.B., Jia W.Y., Yang C.X., *Comparison of rare-earth and hybrid-magnet mover configurations for a permanent magnet synchronous linear motor*, IET Electric Power Applications, vol. 15, no. 3, pp. 321–331 (2021), DOI: 10.1049/elp2.12024.

[13] Zhang Z., Yin S., Wu J., Huang S., *Dynamic and highly energy-efficient virtual network embedding method based on elastic optical networks*, Optical Engineering, vol. 60, no. 12, pp. 2–17 (2021), DOI: 10.1117/1.OE.60.12.126106.

[14] Hong Y., Yoon S., Kim Y.S., Jang H., *System-level virtual sensing method in building energy systems using autoencoder: under the limited sensors and operational datasets*, Applied Energy, vol. 301, no. 1, pp. 2–12 (2021), DOI: 10.1016/j.apenergy.2021.117458.

[15] Tawfiq K.B., Ibrahim M.N., El-Kholy E., Sergeant P., *Refurbishing three-phase synchronous reluctance machines to multiphase machines*, Electrical Engineering, vol. 103, no. 1, pp. 139–152 (2021), DOI: 10.1007/s00202-020-01064-w.

[16] Parvathy M.L., Eshwar K., Thippiripati V.K., *A modified duty-modulated predictive current control for permanent magnet synchronous motor drive*, IET Electric Power Applications, vol. 15, no. 1, pp. 25–38 (2021), DOI: 10.1049/elp2.12004.

[17] Fu R., Cao Y., *Hybrid flux predictor-based predictive flux control of permanent magnet synchronous motor drives*, IET Electric Power Applications, vol. 16, no. 4, pp. 472–482 (2022), DOI: 10.1049/elp2.12168.

[18] Wang Z.Q., Xie S.F., Jin X.F., Shi T.N., Yang M.B., *A novel deadbeat predictive current control of permanent magnet synchronous motor based on oversampling scheme*, IET Electric Power Applications, vol. 15, no. 8, pp. 1029–1044 (2021), DOI: 10.1049/elp2.12078.

[19] Zhu Y., Zhao C., Yin L., Zhou H., Xing C., *A comparative study of switched reluctance motors with a single hase and a novel Synchronous double hase excitation mode*, IET Electric Power Applications, vol. 15, no. 9, pp. 1217–1231 (2021), DOI: 10.1049/elp2.12093.

[20] Lin Y., Sun Y., Wang Y., Cai S., Shen J.X., *Radial electromagnetic force and vibration in synchronous reluctance motors with asymmetric rotor structures*, IET Electric Power Applications, vol. 15, no. 9, pp. 1125–1137 (2021), DOI: 10.1049/elp2.12080.

[21] Liu X.M., Yu H.T., Gerada D., Xu Z.Y., Qin H.B., Jia W.Y., Yang C.X., *Comparison of rare-earth and hybrid-magnet mover configurations for a permanent magnet synchronous linear motor*, IET Electric Power Applications, vol. 15, no. 3, pp. 321–331 (2021), DOI: 10.1049/elp2.12024.

[22] Debnath S., *Fuzzy quadripartitioned neutrosophic soft matrix theory and its decision-making approach*, Journal of Computational and Cognitive Engineering, vol. 1, no. 2, pp. 88–93 (2022).

[23] Yousefi-Talouki A., Pescetto P., Pellegrino G., Boldea L., *Combined Active Flux and High Frequency Injection Methods for Sensorless Direct Flux Vector Control of Synchronous Reluctance Machines*, IEEE Transactions on Power Electronics, vol. 99, no. 1, pp. 1–2 (2017), https://ieeexplore.ieee.org/document/7907329.

[24] Armando E., Bojoi R.I., Guglielmi P., Pellegrino G., *Experimental Identification of the Magnetic Model of Synchronous Machines*, IEEE Transactions on Industry Applications, vol. 49, no. 5, pp. 2116–2125 (2013), DOI: 10.1109/TMAG.2015.2438872.

[25] Varatharajan A., Pellegrino G., *Sensorless Synchronous Reluctance Motor Drives: A General Adaptive Projection Vector Approach for Position Estimation*, IEEE Transactions on Industry Applications, vol. 56, no. 2, pp. 1495–1504 (2020), DOI: 10.1109/TIA.2019.2961986.

[26] Cupertino F., Giangrande P., Pellegrino G., Salvatore L., *End Effects in Linear Tubular Motors and Compensated Position Sensorless Control Based on Pulsating Voltage Injection*, IEEE Transactions on Industrial Electronics, vol. 58, no. 2, pp. 494–502 (2011), DOI: 10.1109/TIE.2010.2046577.

[27] Cupertino F., Pellegrino G., Giangrande P., Salvatore L., *Sensorless Position Control of Permanent-Magnet Motors with Pulsating Current Injection and Compensation of Motor End Effects*, IEEE Transactions on Industry Applications, vol. 47, no. 3, pp. 1371–1379 (2011), DOI: 10.1109/TIA.2011.2126542.

[28] Boazzo B., Pellegrino G., *Model-Based Direct Flux Vector Control of Permanent-Magnet Synchronous Motor Drives*, IEEE Transactions on Industry Applications, vol. 51, no. 4, pp. 3126–3136 (2015), DOI: 10.1109/TIA.2015.2399619.